On the Detection of Icing Conditions at Altitude in Conjunction with Mesoscale Convective Complexes Using Balloon Sondes

CHUNTAO LIU,[a] LAUFEY JÖRGENSDÓTTIR,[b] PAUL WALTER,[b] GARY A. MORRIS,[b,c] JAMES H. FLYNN,[d] AND PAUL KUCERA[e]

[a] *Texas A&M University–Corpus Christi, Corpus Christi, Texas*
[b] *St. Edward's University, Austin, Texas*
[c] *NOAA/Global Monitoring Laboratory, Boulder, Colorado*
[d] *University of Houston, Houston, Texas*
[e] *University Corporation for Atmospheric Research, Boulder, Colorado*

(Manuscript received 21 March 2023, in final form 16 May 2023, accepted 21 June 2023)

ABSTRACT: Balloon-borne radiosondes are launched twice daily at coordinated times worldwide to assist with weather forecasting. Data collection from each flight is usually terminated when the balloon bursts at an altitude above 20 km. This paper highlights cases where the balloon's turnaround occurs at lower altitudes and is associated with ice formation on the balloon, a weather condition of interest to aviation safety. Four examples of such cases are shown, where the balloon oscillates between 3- and 6-km altitude before rising to high altitudes and bursting. This oscillation is due to the accumulation and melting of ice on the balloon, causing the pattern to repeat multiple times. An analysis of National Weather Service radiosonde data over a 5-yr period and a global dataset from the National Centers for Environmental Information from 1980 to 2020 identified that 0.18% of soundings worldwide satisfied these criteria. This indicates that weather conditions important to aviation safety are not rare in the worldwide database. We recommend that soundings that show descent at altitudes lower than typically expected continue to be tracked, particularly given that these up–down-oscillating soundings can provide valuable information for weather forecasting on days with significant precipitation and icing conditions that might lead to aviation safety concerns.

KEYWORDS: Icing; In situ atmospheric observations; Radars/Radar observations; Radiosonde/rawinsonde observations; Cloud Microphysics; Snowmelt/icemelt

1. Introduction

Balloon-borne radiosondes are flown in a coordinated fashion from many sites worldwide, with close to a thousand sites having operational twice-daily flights at 0000 and 1200 UTC, and collect data from the surface until the balloons burst at altitudes exceeding 20 km (e.g., Durre et al. 2006; Wang and Zhang 2008; Ramella Pralungo et al. 2014; Holdridge 2020). Sometimes additional radiosondes are flown for high impact weather conditions such as severe weather events or hurricanes. Balloons typically ascend at ~5 m s^{-1} with instruments (radiosondes) that collect pressure, temperature, relative humidity, and GPS data, including latitude, longitude, and altitude. Wind speed and direction data are derived from changes in the GPS location data. Radiosonde data are assimilated into meteorological models to improve weather forecasts (Hersbach et al. 2020). While data can be collected as the balloon is ascending and descending, the National Weather Service (NWS) typically suspends data collection when flight monitoring software detects a balloon turnaround (which most frequently occurs as the balloon bursts) (Schrab and Caldwell 2010). Thus, archived weather balloon data (e.g., at the University of Wyoming radiosonde archive: https://weather.uwyo.edu/upperair/sounding.html) only include ascending data.

This paper describes in detail a subset of balloon sondes taken as part of scientific field campaigns in which station operators continued monitoring flights after detecting a "turnaround." In each case, the turnaround was not associated with balloon burst, but rather likely with the accumulation of mass (i.e., ice) as the result of particular meteorological conditions near 5 km at which the relative humidity was at or near saturation and the temperature at or near the freezing point of water. Such icing conditions in clouds present aviation safety hazards and remain on the list of high-impact weather factors for aviation meteorology (Gultepe et al. 2019). The balloons subsequently descended, leading to temperature increases, melting of the ice, reduction of the effective balloon and payload mass, and ascended again. The ascent–descent pattern may repeat multiple times before the balloon escapes the area where these conditions exist. More generally, the presence of such conditions, and the meteorological data above these layers, are likely undersampled in the weather balloon database as a result of the standard NWS data collection practices, which exclude all data after the first turnaround point.

The conditions of balloon icing have been well documented in the past. Ciesielski et al. (2014) reported a small fraction (~5%) of slowly rising balloons, as well as a few early terminations of radiosonde flights, likely due to icing in tropical convective systems during the Dynamics of the Madden–Julian Oscillation (DYNAMO; Yoneyama et al. 2013) field campaign. Further, Waugh and Schuur (2018) showed direct evidence of the icing through a layer with supercooled liquid using a GoPro camera attached to a radiosonde flying into a winter storm. To cause a balloon oscillation, a condition with both significant icing

Corresponding author: Chuntao Liu, chuntao.liu@tamucc.edu

DOI: 10.1175/MWR-D-23-0062.1

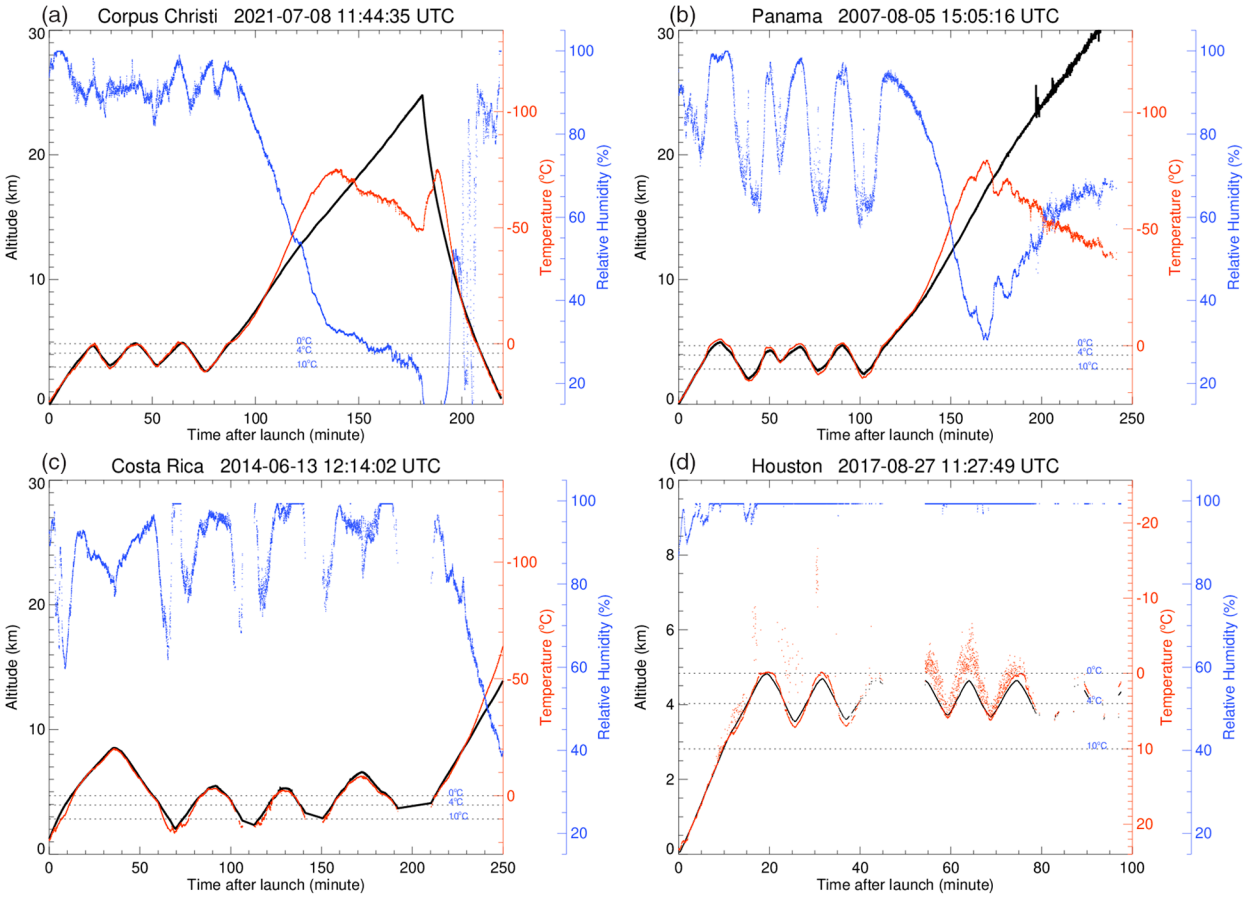

FIG. 1. Time evolution of temperature (red), altitude (black), and relative humidity (blue) during four unusual weather balloon launches over (a) Corpus Christi, (b) Panama, (c) Costa Rica, and (d) Houston.

and melting is required. A recent example of these meteorological conditions occurred on 8 July 2021. An ozonesonde was released at 1144 UTC (0644 CDT) at Texas A&M University–Corpus Christi (27.72°N, 97.33°W). The balloon payload included a standard radiosonde with an additional instrument that measures ozone, an electrochemical concentration cell (ECC) ozonesonde (Komhyr 1969). The flight occurred during light rain as a tropical system brought heavy precipitation to the Corpus Christi area. Figure 1 shows the altitude of the balloon (black), the temperature (red), and relative humidity (blue) as functions of time for four flights that will be discussed in more detail in this paper. Typically, the balloon rises at a nearly constant rate until burst, which usually occurs between 25- and 35-km altitude, depending on the size of the balloon used. In this case, however, instead of rising continuously to burst, the balloon altitude oscillated between 3 and 5 km, as can be seen in Fig. 1a.

This type of oscillating behavior has been observed on several occasions [e.g., in Panama during the 2007 Tropical Composition, Cloud, and Climate Coupling (TC4) campaign, as discussed in Morris et al. (2010), in Magnolia, Texas, during Hurricane Harvey in 2017, and in Costa Rica in 2014]. All sites reported similar conditions at the time of these flights: they took place in June–August (Northern Hemisphere summertime) in subtropical or tropical regions in or near areas of active convection and precipitation. Our analysis demonstrates that the most plausible explanation for the oscillations is the mass accumulation of ice on the balloon and payload as it ascends through saturated air near the freezing point of water, causing the balloon to slow its ascent before then descending. As the balloon descends, the temperatures rise, melting the ice, reducing the mass, and allowing the balloon to start ascending again. If the balloon has not moved laterally with respect to these meteorological conditions and the meteorological conditions have not changed, the oscillating behavior may repeat. We analyze this behavior for these four cases in more detail in section 3.

To better understand the scope and prevalence of such meteorological conditions, we used data from the U.S. National Weather Service (NWS) operational radiosonde database and the Integrated Global Radiosonde Archive (IGRA; Durre et al. 2006, 2018). We analyzed soundings over a 5-yr period from August 2016 to July 2021 to identify profiles during which conditions were favorable for ice to accumulate on the balloon, and the balloon showed an initial descent beginning at altitudes below 7 km. Since the NWS only collects data until the initial

turnaround, these flights will appear to have truncated records (i.e., data will only be reported from the ground to the first turnaround point at ~4–7-km altitude). As such, it is impossible to determine whether those balloons oscillated as the example flights in this paper did. However, we estimate the occurrence of such conditions by the frequency of those soundings that cut off early at altitudes with near-saturated relative humidity and temperatures near the freezing point of water. Such flights are candidates for oscillating behavior. These data provide valuable insights into highly convective environments that can benefit weather forecasting and improve aviation safety in the vicinity of such storm systems. The termination of data collection on these flights at the altitude of the first turnaround represents a missed opportunity to collect valuable data in conjunction with these conditions, particularly regarding aviation safety and weather forecasting.

2. Measurements

a. Radiosondes

The radiosonde measures pressure, temperature, and humidity, and for more recent soundings, also GPS latitude, longitude, and altitude. Changes in latitude and longitude with time are used to derive the wind speed and direction data. Radiosondes typically transmit data every second. The data are transmitted to and recorded at the surface using an antenna, receiver, and software system, making it unnecessary to recover the payload after the flight to obtain the data. In this paper, three out of four examples of oscillating flights deployed an InterMet (iMet)-1RSB radiosonde, while the fourth, Corpus Christi, used the newer iMet-4RSB radiosonde.

The National Weather Service sites and other global sites release radiosondes on weather balloons twice daily (at 0000 and 1200 UTC) (Dirksen et al. 2014; von Rohden et al. 2022). The Integrated Global Radiosonde Archive (IGRA; Durre et al. 2006) includes balloon radiosonde observations from the early twentieth century to the present from more than 2800 stations around the globe. Though there are a large variety of instruments, balloon setups, and launching environments over different countries (Gaffen 1994; Miloshevich et al. 2009), this dataset archive compiles the historical radiosonde data in a single data format, simplifying analysis efforts of the records. Analysis of the IGRA archive allows us to examine the global occurrence of radiosonde profiles ending at low altitudes.

The ECC ozonesonde consists of a small mechanical pump that bubbles samples of ambient air outside of the payload through a cathode solution consisting of a diluted (0.5%–2.0%) concentration of potassium iodide (KI). The ozone concentration can be determined by measuring the electrical current flowing between the solution cells and knowing the volume flow rate of the pump, the ambient pressure, and the pump temperature (Komhyr 1969). Details on the ozonesonde and best practices for preparing, calibrating, and flying ozonesondes can be found in the latest report from the Assessment of Standard Operating Procedures for OzoneSondes (ASOPOS) group (Smit et al. 2021). There are two leading manufacturers of ozonesondes: EnSci and Science Pump. All the flights with ozonesondes described in this paper used the En-Sci 2Z series ozonesonde pumps.

b. Infrared brightness temperatures

To describe the cloud systems that balloon sondes flew through in all four cases, the geostationary satellite infrared (IR) images are used. The combined IR product is created by merging the pixel resolution (~4 km) IR satellite data from all available geostationary meteorological satellites into a global (60°N–60°S) grid every half-hour (Janowiak et al. 2001).

c. Radar

To better understand the meteorological conditions around the time of the unusual oscillating balloon flights, we present radar data collocated at two of the balloon release sites: Corpus Christi and Panama. We analyzed data from a collocated Micro Rain Radar (MRR) and the Multi-Radar Multi-Sensor (MRMS) system for the Corpus Christi case. The MRR instrument is a Biral/Metek 24 GHz (K-band) continuous wave, vertical pointing profiling Doppler radar that derives several rain parameters from measured spectral power backscatter intensity (Klugmann et al. 1996). The radar can be used to measure rain rate, liquid water content and drop size distribution in the range of 0.25–4.53 mm from near the ground to several hundred meters. The MRR is located at the launch site in Corpus Christi and within 10 km of where the balloon oscillated. The MRMS system combines data streams from more than 150 radars, satellites, surface observations, upper-air observations, lightning reports, rain gauges and numerical weather prediction models to produce over 100 products at 1-km spatial resolution every 2 min over the continental United States (Zhang et al. 2016; Smith et al. 2016).

For the Panama example, we use data from the NASA polarimetric Doppler weather radar (NPOL), an S-band system operating at 2.8 GHz (10-cm wavelength), deployed adjacent to the balloon release site. Because this system does not work well when the antenna is wet (Theisen et al. 2009), periods with active rain are excluded from the analysis. During the TC-4 campaign in Panama, NPOL scanned with a spatial resolution of 200 m using a 12-tilt strategy (elevation angles from 0.7° to 23.3°) with a temporal resolution of 10 min. Among the many parameters measured, NPOL, like MMS, reports radar reflectivity (DZ). For further details on the TC-4 deployment of the NPOL radar, see Morris et al. (2010).

3. Oscillating flight observations

In this section, we describe and analyze four flights during which the balloon oscillated up and down between 2.5–3.5 km at the lower limit and 4.5–6.0 km at the upper limit. These flights occurred at Corpus Christi, Texas; Magnolia, Texas; Las Tablas, Panama; and San Jose, Costa Rica. The lower limits of the oscillations were characterized by temperatures of 7° to 12°C, while the upper limits were characterized by temperatures of −3° to 0°C. The two tropical sites (Costa Rica and Panama) showed relative humidity values near the bottom of each oscillation below 80% and values at the top >90%. The two subtropical sites, Magnolia and Corpus Christi, showed little to no variability

TABLE 1. Details about the balloon sizes and payloads on the four case studies of oscillating balloon flights described in this paper.

Date	Time (UTC)	Location	Lat, lon, alt	Payload	Payload weight (kg)	Balloon size (kg)
8 Jul 2021	1144–1523	Corpus Christi, TX	27.7°N, 97.3°W, 5 m MSL	Ozonesonde + iMet-4 Radiosonde	1.5	0.8
5 Aug 2007	1505–1906	Las Tablas, Panama	7.8°N, 80.3°W, 5 m MSL	Ozonesonde + RS80 Radiosonde	1.5	1.2
13 Jun 2014	1214–1636	San Jose, Costa Rica	9.9°N, 84.0°W, 1200 m MSL	Ozonesonde + CFH + iMet-1 Radiosonde	3.5	1.2
27 Aug 2017	1142–1309	Magnolia, TX	30.2°N, 95.8°W, 30 m MSL	iMet-1 Radiosonde	0.4	0.35

in the relative humidity in the vertical oscillations. A more detailed description of each flight is listed in Table 1.

a. Corpus Christi, Texas, sounding

On 8 July 2021, an ozonesonde was released in light rain at 1144 UTC at Texas A&M University–Corpus Christi (27.72°N, 97.33°W, 5 m MSL), located on the Texas Gulf Coast. A tropical system centered just off the coast brought heavy precipitation into the area. This flight took place during an ozonesonde training workshop in preparation for the first part of the Dynamics and Chemistry of the Summer Stratosphere (DCOTSS) campaign during the summer of 2021. The mission included coordinated aircraft and balloon sonde measurements to examine the impact of deep, midlatitude convection that overshoots the tropopause and injects material into the lower stratosphere in conjunction with the North American monsoon anticyclone (Homeyer et al. 2023).

The payload for this flight included a standard EnSci ozonesonde in a cubic Styrofoam box (~30 cm per side) with an iMet-4 radiosonde affixed to one side of the box, suspended from an 800-g latex balloon via a payout reel (which gradually pays out string to separate the balloon from the payload, becoming fully extended at ~45-m length below the balloon about 10 min into the flight) and parachute (~80-cm diameter when open fully, but folded on ascent). The total mass of the payload is ~1.5 kg.

Figure 1a shows the altitude, temperature, and relative humidity as a function of time for this balloon flight. The balloon initially ascended for ~20 min to an altitude of 4.71 km MSL, at which point the air temperature had dropped to −0.2°C and the relative humidity (RH) had climbed to 97%. The balloon began descending. Temperatures increased to 10.7°C and RH dropped to ~90% by the time it reached 3.15 km MSL, at which point it began to rise again. The second ascent peaked about 20 min after the first near 4.93 km MSL (~0.4°C, RH ~ 98%), and the second descent reached a minimum altitude of 3.17 km MSL again (~9.9°C, RH ~ 87%) about 9 min later. The third ascent peaked about 20 min after the second peak, reaching 4.97 km MSL again (~0.2°C, RH ~ 97%), and the third descent minimum altitude was 2.67 km MSL (~12.0°C, RH ~ 95%). On its final ascent, the temperature was 0.0°C at 4.74 km MSL about 12 min after the last peak altitude, with RH ~ 97% still, but the balloon did not descend this time and instead continued rising to a burst altitude around 25 km.

Figure 2a shows the trajectory of this balloon superimposed on the infrared (IR) brightness temperature in the region at around 1200 UTC, about 15 min after the release of the balloon and nearly coincident with the beginning of the first descent. The balloon trajectory is in a region with brightness temperatures greater than −60°C and to the northwest of the convective region with a minimum brightness temperature of −75°C. Therefore, the balloon was drifting through the large stratiform region of a mesoscale convective system (MCS). This is further verified by the MRMS radar reflectivity at 4 km at four different times during the balloon oscillation (Figs. 3a–d). The balloon drifted over a region with relatively homogeneous radar reflectivity around 30–35 dBZ at 4 km, and then it continued rising after drifting to a region with lower reflectivity around 20–25 dBZ.

The time series of radar reflectivity profiles following the balloon trajectory is shown in Fig. 4a, confirming that the balloon oscillated in the region with 30–35 dBZ near the freezing level and continued rising after escaping from the high reflectivity region (from dark to light blue). However, ground-based radar does not have a sufficient vertical resolution to describe the structure of the system where the balloon oscillated through. To further describe the vertical structure of the system, Fig. 5 shows the radar reflectivity and Doppler velocity observed by the MRR at the launch site, which is within 10 km of the oscillating balloon. Because the stratiform precipitating region was homogeneous and slowly propagated over the launch site (Fig. 3), the K-band vertically pointing radar captured the vertical structure of the system near the freezing level in greater detail. The "bright band" of high radar reflectivity between 2° and 4°C in Fig. 5a shows a typical feature of the stratiform region of the MCS. The reflectivity increases toward the surface, corresponding to the growth of the raindrops through the collision–coalescence process, though this could also be from the radar signal attenuation. The low variability of the reflectivity and Doppler velocity with time (Figs. 5a,b) suggests that the balloon oscillated in the stratiform region with a homogeneous vertical air motion. A mesoscale downdraft can be prevalent in the stratiform region of a large MCS (Houze 2018) and it is possible that air vertical motion can indeed push down a balloon (Wang et al. 2009). However, the downdraft is not the reason for this case. Figure 5b shows that the balloon turned around at the freezing level with low radar reflectivity (20–25 dBZ). The Doppler velocity is less than 3 m s^{-1} and consistent with falling ice particles, possibly with small near-freezing liquid drops to make ice particles stickier. The terminal velocity increased to 6–9 m s^{-1} at temperatures warmer than 4°C, where ice fully melted into raindrops. This vertical structure was quite uniform during the event

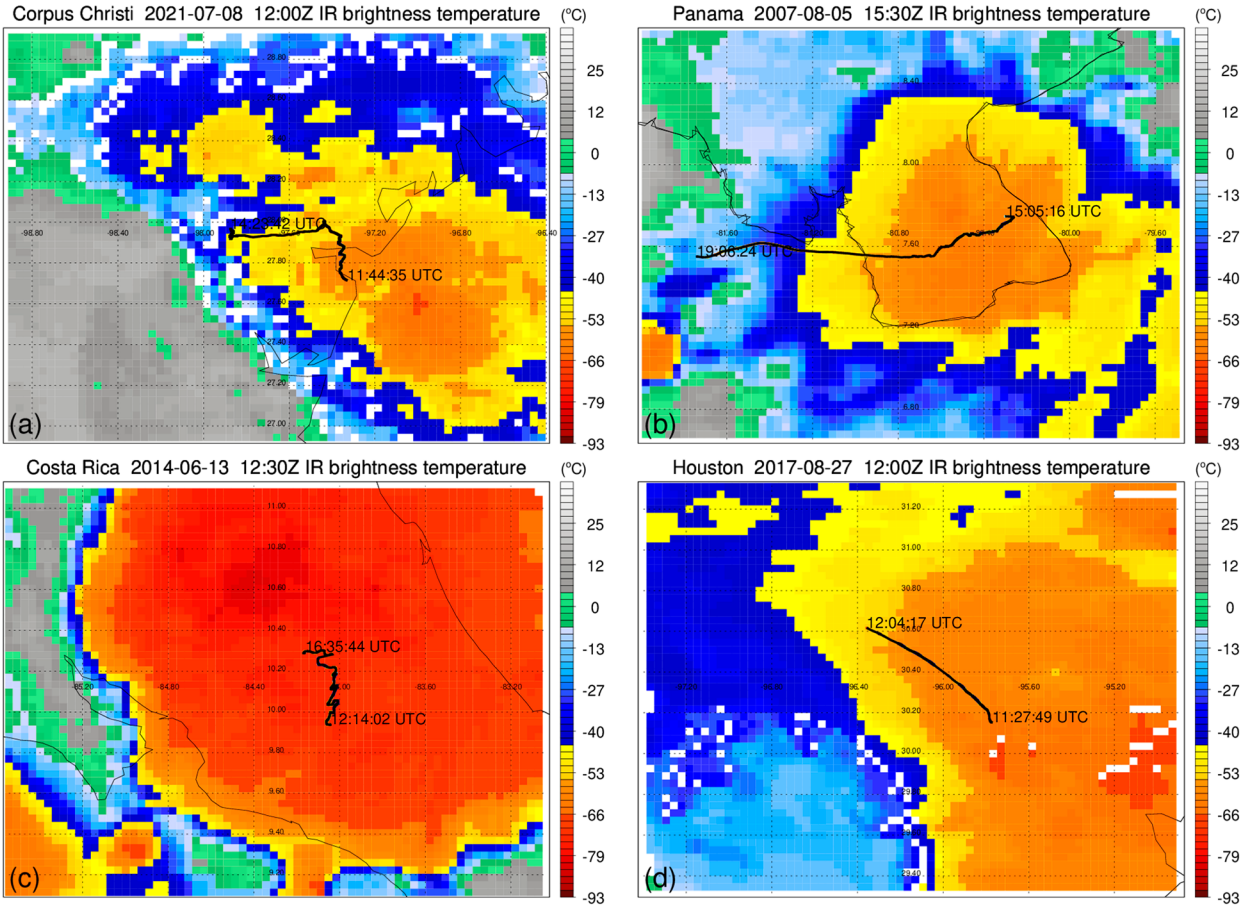

FIG. 2. Infrared brightness temperature field in the middle of the balloon flights. The balloon flight trajectories are superimposed on the infrared brightness temperature field for a time in the middle of the balloon flights. The black line traces the balloon paths. The thin black lines show the coast lines and country borders.

period. Therefore, the most likely explanation for the balloon oscillation is the collection of ice particles and melting.

To closely examine the thermodynamic environment of the oscillation of the balloon, Fig. 6a shows the rising rate of the balloon as the function of temperature, with negative rise rates corresponding to the balloon descending after reaching the freezing point, then descending through warmer air until the ice melts, leading to the rise rates becoming positive again. The balloon repeated this up–down pattern three additional times before ascending to a burst altitude of ~25 km, indicated by the repeating cycles around 0°–10°C colored by the minutes elapsed since launch. The first up–down cycle can be seen in green, the second and third in blue and the fourth in yellow. The balloon rising and descending rates were around 4.5 m s^{-1}. During the first turnaround, the rising rate started to decrease at a temperature around 0°–2°C, implying that icing and supercooled liquid can occur at a temperature even warmer than the freezing temperature. The descending rate started to decrease at a temperature range of 8°–12°C, showing variable conditions for melted ice falling off the balloon and payload. Figures 7a and 7b (cross symbols) shows that during the event, the horizontal wind was relatively weak (~5 m s^{-1}), which is consistent with the relatively homogeneous stratiform region. Figure 7c shows the balloon ascended through a cloud layer with close to 100% RH between 13° and 20°C. Between 0° and 13°C, the ambient air was subsaturated until the freezing level. Here we should question the quality of the RH measurements during the icing. The subsaturated layer right below the freezing level may not be reliable.

We may derive the acceleration rate along the balloon trajectory by using the variation of the rise rate with time. The histogram of the acceleration rates of this case is shown in Fig. 7d. The acceleration rates have more negative values at temperatures just below freezing and more positive values at temperatures 5°–10°C. All these suggest that the explanation for this oscillating behavior is associated with the accumulation of ice on the balloon and payload (causing downward acceleration of the motion) and subsequent melting of the ice (resulting in upward acceleration). Using the acceleration and the information of the balloon and payload and with some assumptions and applying Newton's second law with air drag, we can estimate the mass of ice load over the balloon and payload during the event (see the appendix). Figure 8 shows that more than 1.5 kg of ice accumulation on the balloon was required to cause a descent at

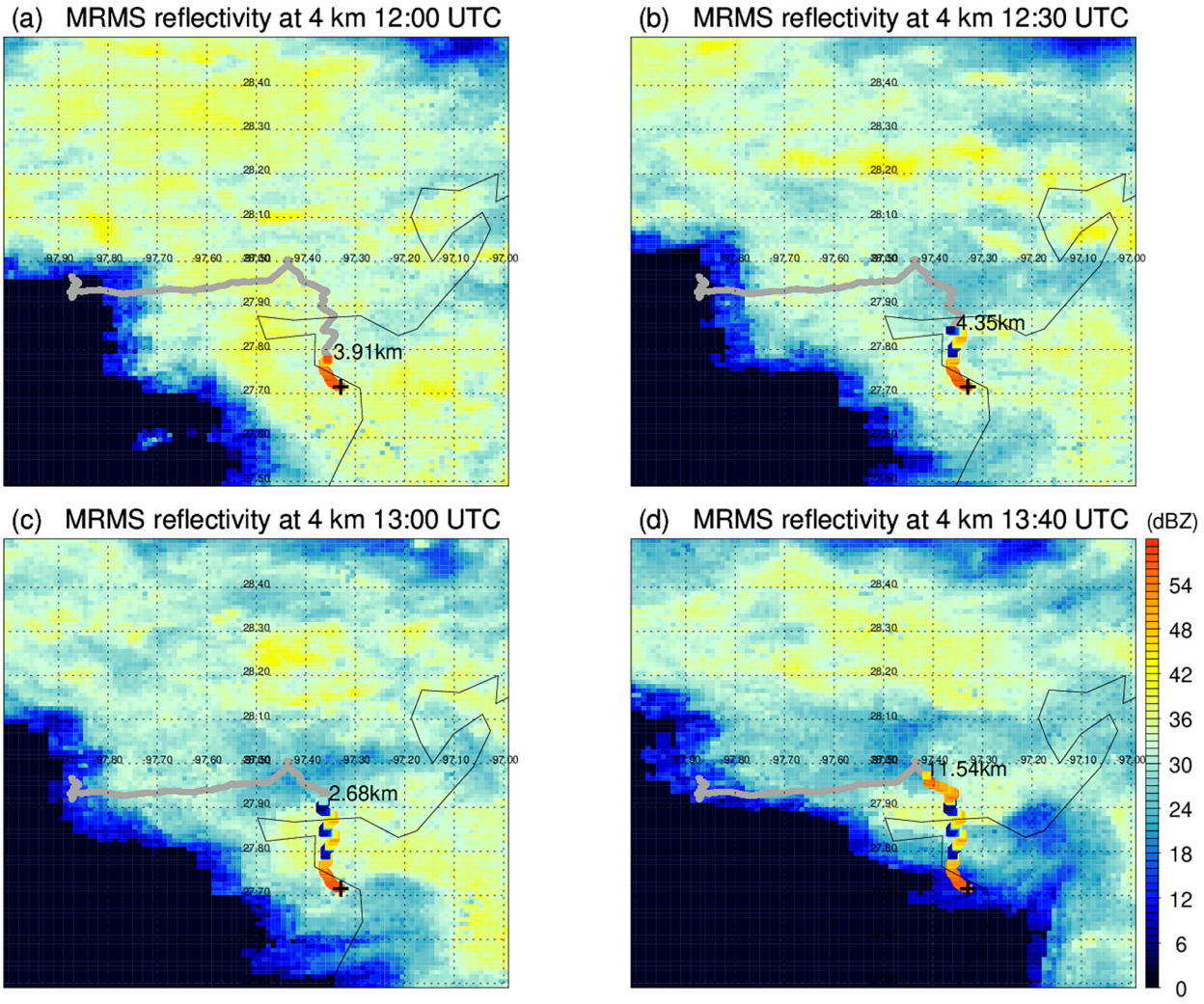

FIG. 3. Snapshots of MRMS-interpolated radar reflectivity at 4 km during the balloon flight at Corpus Christi. The balloon flight trajectories are shown as gray lines. The color of the line represents the rising rate (negative in blue, positive in orange) of the balloon before the time of the radar image. The altitude of the balloon at the radar image time is labeled. The location of the launch site is marked with a black cross. Note that the balloon was flying in a horizontally uniform region during the up-and-down cycles.

~4.5 m s^{-1}. Because the amount of ice increases significantly from 2° to 0°C, we estimated the ice accumulation rate from the balloon deceleration rates in this layer. After estimating the surface area of the payload and the surface area of the balloon considering the volume expansion, the icing rate at 0°–2°C is estimated at 0.17 g m^{-2} s^{-1}.

b. *Las Tablas, Panama, 2007 sounding*

Another example of an oscillating balloon sounding occurred during a flight from Las Tablas, Panama, in 2007, as was reported by Morris et al. (2010). The balloon flight was part of the TC4 mission, which took place from 13 July to 9 August 2007 (Toon et al. 2010). At the time and place of release on 5 August 2007, light rain was falling, the temperature was ~24°C, and the relative humidity was ~96% at the surface. These conditions are like those observed in conjunction with the Corpus Christi sounding.

This flight used a 1200-g balloon with a payload that included a standard ozonesonde, a Vaisala RS80 radiosonde, and a GPS unit integrated into the lid of the payload's Styrofoam box (total payload mass of ~1.5 kg). The balloon ascended through the edge of a dissipating convective system that moved onshore from the east and oscillated five times between 2.5 and 5.1 km over nearly 2 h before resuming a normal ascent. Figure 1b shows the time series of altitude, temperature, and relative humidity measured by the radiosonde. The initial ascent reached 5.1 km with a temperature of −2.9°C and a relative humidity greater than 98% before the balloon began descending. Over the next 15 min, the balloon descended to 2.2 km and the temperature reached 15.1°C, with relative humidity values dropping to 69%. The second ascent peaked at 4.5 km about 12 min later with a temperature of 0.7°C and a relative humidity > 97%. The second descent took about 6 min, reaching a minimum altitude of 3.6 km with a

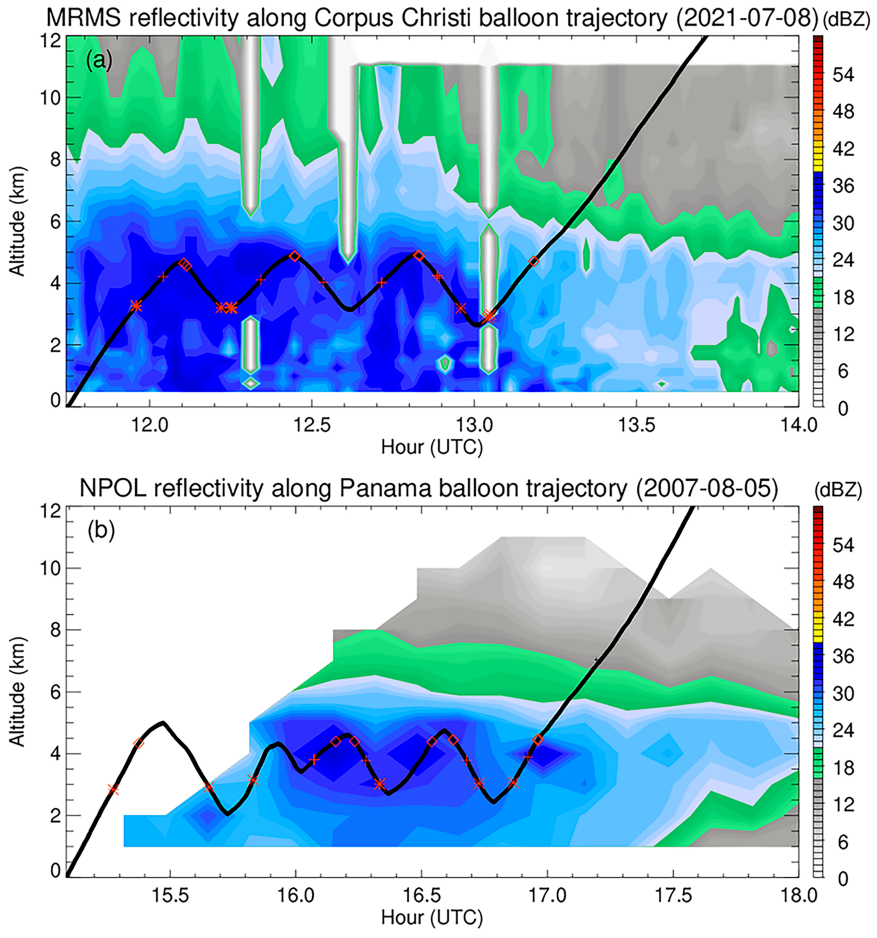

FIG. 4. Field of vertical radar reflectivity profiles at the time and location of balloon trajectory derived from (a) MRMS and (b) NPOL 3D reflectivity products. The black line shows the altitude of the balloon. The altitudes at 0°, 4°, and 10°C are marked with diamonds, crosses, and asterisks, respectively, along the trajectory.

temperature of 7.3°C and a relative humidity of 73%. The third ascent peaked at 4.7 km about 10 min later with a temperature of −0.8°C and a relative humidity of 98%. The third descent took about 10 min, reaching a minimum altitude of 2.9 km with a temperature of 12.3°C and a relative humidity of 66%. The fourth ascent peaked at 4.9 km about 14 min later with a temperature of −1.2°C and a relative humidity of 97%. The fourth descent took about 11 min, reaching a minimum altitude of 2.6 km with a temperature of 13.1°C and a relative humidity of 62%. On its final ascent, as the balloon passed through the 0°C temperature near 4.6 km, the relative humidity reached only 93%. The balloon continued upward on a more typical ascent with a monotonic rise rate until bursting above 30 km some 2 h later.

Figure 2b shows the trajectory of the balloon overlaid on the map of IR brightness temperature at 1530 UTC, approximately 25 min after the release of the balloon. Again, the balloon remains in the stratiform region of an MCS with IR brightness temperatures warmer than −60°C. This convective system rapidly dissipated as it came on shore from the ESE of Las Tablas. Figure 4b shows the vertical position of the balloon and the NPOL reflectivity versus altitude as a function of time for 5 August 2007. Similar to the Corpus Christi event, the balloon appears "trapped" in regions with reflectivity values greater than 30 dBZ at the freezing altitude near 5.0 km and "escapes" when the reflectivity value at this level drops to below 25 dBZ. The horizontal wind was also weak (~5 m s^{-1}) during the oscillation (Figs. 9a,b). Unlike the Corpus Christi case, the layer between 0° and 10°C is much dryer, with 60%–70% RH in the Panama case compared to ~90% RH in the Corpus Christi case (Fig. 9c).

c. *San Jose, Costa Rica, 2014 sounding*

A balloon payload was released from San Pedro in San Jose, Costa Rica, at 0614 CST (1214 UTC) on 13 June 2014. The payload for this flight included a standard EnSci ozonesonde in the Styrofoam box with an iMet radiosonde attached (described previously), a cryogenic frost point hygrometer (CFH; Vömel et al. 2007; Hurst et al. 2011), a payout reel and parachute (total payload mass ~ 3.5 kg), all suspended from a 1200-g latex balloon.

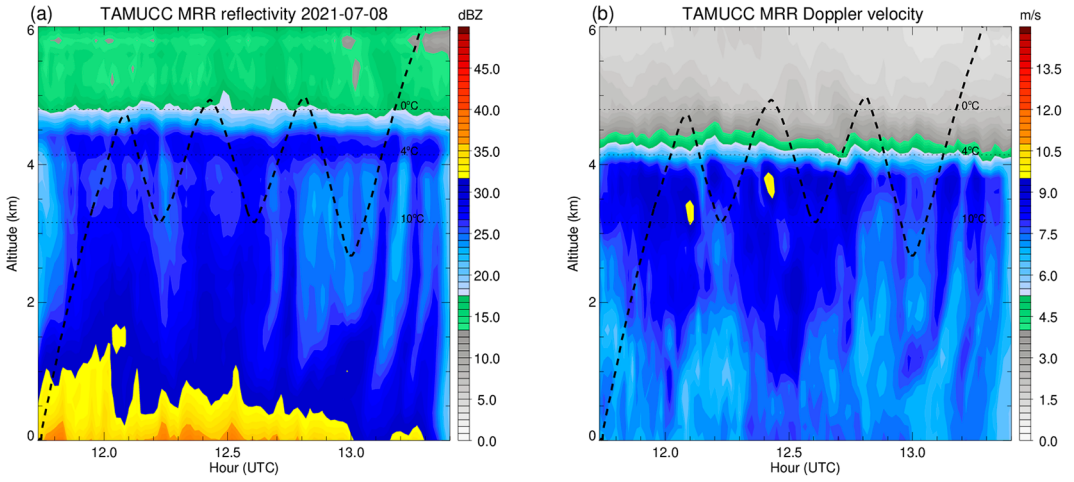

FIG. 5. (a) Radar reflectivity during the balloon going up and down from a vertically pointing Ka-band Micro Rain Radar (MRR) at the balloon launching site (Texas A&M–Corpus Christi campus). (b) Doppler velocity from MRR. The altitude of the balloon is overplotted with a dashed line. The mean altitudes at 0°, 4°, and 10°C are indicated with the dotted lines. Note that the balloon drifted within 20 km from the launch site during the period.

At the time of balloon release from the surface, the temperature was 20°C with overcast conditions. Figure 1c shows the altitude, temperature, and relative humidity as functions of time for this balloon flight. On the initial ascent, about 13 min after its release, the balloon temperature dropped below 0°C at 4.9 km, with a relative humidity recorded at 88% by the iMet radiosonde and a frost-point temperature of −2.5°C as measured by the CFH instrument. During that part of the ascent, rise rates dropped from ~6 m s^{-1} in the first kilometer above the surface to ~3 m s^{-1} at 5 km. Over an ~8-min period beginning ~34 min after release, the balloon's rise rate falls from ~+2.5 to ~−3.2 m s^{-1}. For much of the ascent, temperatures were within 1.0°C of the frost-point temperature reported by the CFH. However, around the top of the first ascent, temperatures briefly dipped below the frost-point temperature by 1°–2°C for ~30 s before returning to 0°–1°C above the frost-point temperature. About 40 min after release, the balloon reached an altitude of ~8.5 km MSL. For the next ~21 min, the balloon descended at 3–4 m s^{-1}, crossing the 0°C level near 4.8 km. Temperatures increased on the descent and exceeded the freezing from 2.0° to 9.6°C by 2.9 km before humidity levels began to rise again near the bottom of the first descent, which took another 13 min and occurred at an altitude of ~2.0 km MSL. Near the bottom of the first oscillation, the rise rate changed rapidly from −5.0 to −2.8 m s^{-1} over 1 min, was constant for ~20 s, then rapidly changed from −2.8 to +3.9 m s^{-1} over ~40 s. Temperatures near the bottom of the first descent were above 15°C. The balloon then oscillated three more times between 2 and 7 km before ascending to a burst altitude of 17 km. However, much of the data after the minimum height turnarounds was not recorded on this flight (due to line-of-site transmission issues near the horizon in the mountainous terrain). Near the top of the second ascent, the rise rate slowed from ~3.6 to ~1.0 m s^{-1} over ~90 s, remained fairly constant in the range of 0.6–1.0 m s^{-1} for the next ~150 s, then over the next 90 s, dropped to −2.5 m s^{-1}.

Of the four soundings discussed, the sounding from San Jose occurred the farthest from the coast. San Jose is located in the tropics near the center of Costa Rica in a valley between two volcanically active mountain ranges. It also flowed through an MCS with much colder IR brightness temperatures than the other three cases (Fig. 2c). Though the balloon's trajectory seems outside of the convective core region, the colder IR brightness temperature would imply a deeper cloud and perhaps an early stage of the MCS. Supercooled liquid could exist at a colder temperature in relatively fresh dying convection/stratiform regions. Therefore, the icing occurred at a relatively colder temperature, which led to a higher turnaround altitude for this case.

d. Magnolia, Texas, 2017 sounding during Hurricane Harvey

An oscillating sounding was also observed in a launch from the Houston area on 27 August 2017 during Hurricane Harvey. Harvey was a category-4 hurricane that made landfall in Texas on 25 August and remained near Houston through 29 August with devastating impacts (van Oldenborgh et al. 2018). This sounding differs from the others described above as the payload only included an iMet radiosonde (~260-g mass) attached directly to a 150-g balloon. The balloon oscillated in an ascending and descending pattern until the signal was lost (see Fig. 1d). However, from the available data, the balloon oscillated multiple times between altitudes of 3 and 5 km with temperatures between 0° and 10°C and at a relative humidity of ~100%.

Figure 1d shows the altitude of the balloon, the temperature, and the relative humidity as a function of time into the flight. The first ascent of the balloon reached a peak altitude of 4.8 km about 20 min after release, with a temperature of −0.2°C. Once the balloon ascended above 0.7 km, relative humidity measurements exceeded 98% for the duration of the flight, often with the radiosonde reporting 100% RH. Over the next 6 min, the balloon descended to a minimum altitude

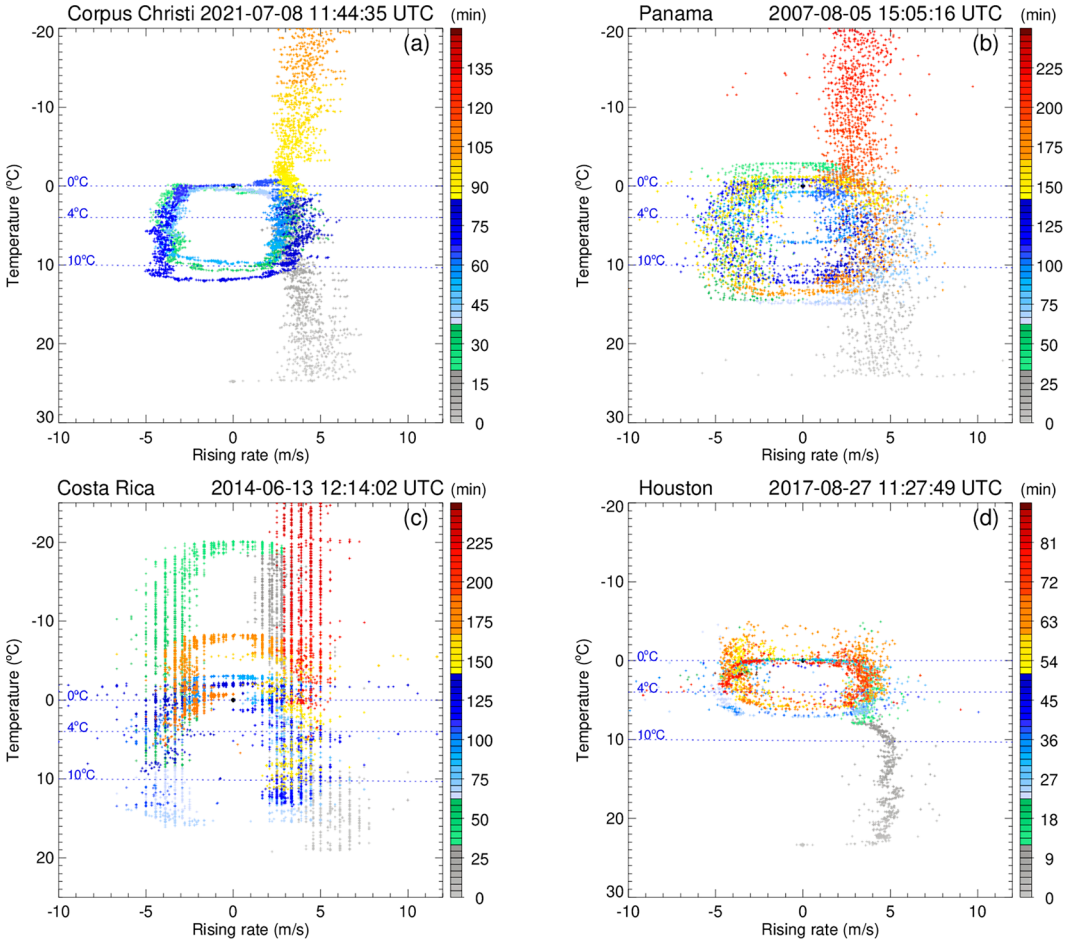

FIG. 6. Scatterplots of the rising speed as a function of temperature during flights over (a) Corpus Christi, (b) Panama, (c) Costa Rica, and (d) Houston. The color of the symbol represents the time after the launch.

of 3.6 km with a temperature of 7.1°C. The second ascent peaked at 4.7 km about 6 min later with a temperature of −0.2°C and the RH still 100%. The second descent reached 3.6 km 5 min later with a temperature of 7.0°C and an RH of 100%. The third ascent peaked at 4.7 km 6 min later with a temperature of 0.0°C. The next cycle occurred mostly during a period of radio drop-out, but the fourth descent bottomed out near 3.7 km with a temperature of 6.0°C some 16 min after the third peak altitude had been attained. The temperature data became significantly noisier during and subsequent to the fourth descent. The fifth ascent peaked at 4.6 km some 5 min later with minimum temperatures in the −3° to −6°C range. The fifth descent reached 3.7 km about 5 min later with a maximum temperature just above 6°C. The sixth ascent reached 4.6 km, again about 5 min later, with a minimum temperature of 0° to −2°C. The balloon began to descend again, but the signal became unreliable before reaching a minimum altitude. Intermittent data some 20 min later indicate that the balloon was still trapped in the layer between 3.5 and 5.0 km. Communications were lost 110 min after the initial release of the balloon.

Figure 2d shows the balloon flight path superimposed on the IR brightness temperature map for Houston at 1200 UTC, approximately 32 min after the release of the balloon from the surface. As for the Corpus Christi and Panama cases, the balloon trajectory was to the NW of the deepest convection (indicated by the coldest IR brightness temperatures at −68°C). The balloon remained in a region of the storm with brightness temperatures greater than −60°C but well away from the edge of the system, which suggests vertical motion (i.e., downdrafts) is an unlikely explanation for the observations.

4. Analysis of operational upper-air soundings

a. National Weather Service radiosonde database (2016–21)

The National Weather Service launches weather balloons with a radiosonde instrument twice daily at ~0000 and ~1200 UTC from more than 80 sites. To determine how frequently oscillating behavior occurs for weather balloon launches, we analyzed NWS radiosonde data from 78 sites throughout the United States over a 5-yr period (August 2016–July 2021). The station

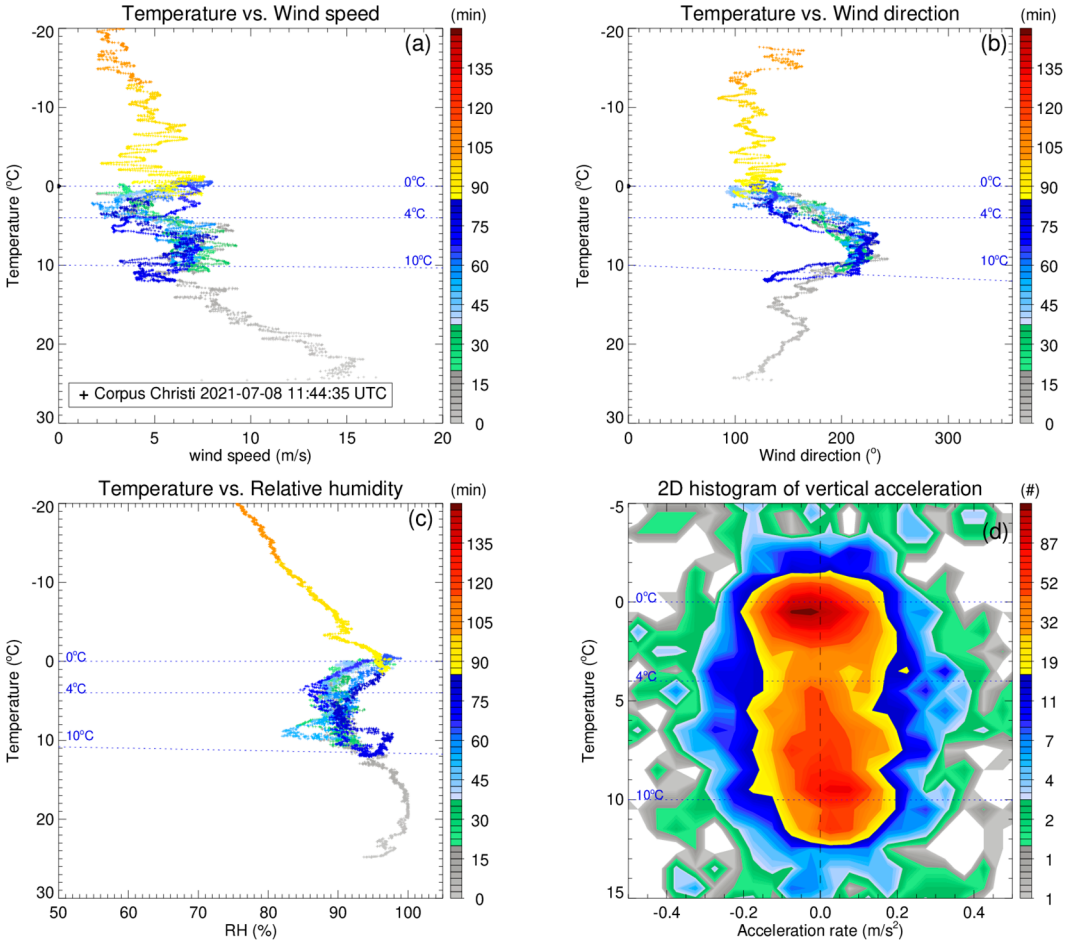

FIG. 7. Scatterplots of the (a) wind speed, (b) wind direction, and (c) relative humidity as a function of temperature during flights over Corpus Christi. The color bars in (a)–(c) represent the time after the launch. (d) A two-dimensional histogram of vertical acceleration.

locations and the number of possible up–down-oscillating cases for each station are shown in Fig. 10a. The NWS soundings only track the ascent, and thus data from a profile end once the payload starts to descend. The cases with a potential to be an oscillating balloon are selected for which the flight data terminated at or below an altitude of 7 km MSL with RH > 80% and a temperature between −10° and 10°C at the termination of sounding. Out of the 267 029 sounding profiles, we identified 295 soundings that satisfied those conditions. We then individually examined each of the 295 soundings and excluded cases where the temperature was far from the freezing point and relative humidity was relatively low. We also removed instances initially identified erroneously due to changes midprofile to the data formatting. These removals reduce the number of soundings identified as potential oscillating cases over the 5-yr period to 170.

In general, the distribution of stations for which these flights occurred was near the coast and inland of the Gulf of Mexico. This area is often impacted by tropical weather systems and regularly experiences other, more localized severe weather events. Figure 10b shows the number of cases each month, with annual analysis periods running from August to July of the following year (i.e., year 1 includes samples in August 2016–July 2017). The black line indicates the average trend for all years. The potential oscillating cases are more frequent during April–October, months with a higher likelihood of tropical systems with significant precipitation, than November–March.

b. *NCEI radiosonde database (1980–2020)*

We expanded the analysis of the occurrence of early terminated flights using the 2800 station database of global radiosonde stations compiled at the NCEI. Figure 11a depicts a histogram of the number of flights that terminated at altitudes corresponding to the temperatures indicated. Focusing on the warmer side of the distribution, we note a shoulder appearing in the −10° to 0°C temperature range (~0.18% of all samples). The distribution of flights terminating above 0°C drops off rapidly at that point. Therefore, the shape of the distribution implies a physical process occurring near the freezing point that results in the enhanced termination of data recording for these flights.

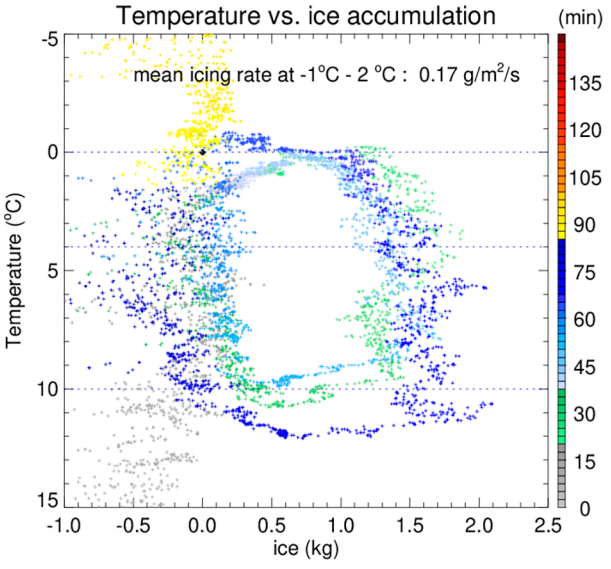

FIG. 8. Estimated amount of ice accumulation on the balloon package during the ozonesonde flight at Corpus Christi.

Figure 11b displays the global distribution of the frequency of such flights. Relative enhancements in the frequency of these early terminated flights are shown in the southeastern United States, Central America, the Bahamas, the Mediterranean coast, and throughout India, Indonesia, and the Philippines. Note that the early termination of the balloon flight could be related to the quality of the balloons, the gas (helium or hydrogen) used to fill the balloons, and the weather systems balloon rising through. The regions with a higher frequency of early terminated flights are mainly in the tropics and subtropics and are also known for frequent MCSs (Houze 2018; Zipser et al. 2006). The enhancements in the southeastern United States in Fig. 11 are consistent with what was found in the analysis of the 5-yr radiosonde record from the National Weather Service. Because there is a relatively stronger diurnal variation of MCSs over land than over ocean (e.g., Nesbitt and Zipser 2003; Houze 2018), soundings released at the two universal times could be in the diurnal peak of MCS in some regions, but in the valley in other regions depending on their longitude. Therefore, the diurnal sampling must be considered while intercomparing stations in Fig. 11b. Also notice that many cases are found in high latitude that could be associated with winter storms, where icing condition occurs frequently in subfreezing layers even below the melting layer (Waugh and Schuur 2018).

5. Discussion and conclusions

While the four case-study soundings described here display similar characteristics of oscillating behavior, there are some variations in the period of oscillation among them. The shortest time between each oscillation occurred for the Houston sounding (~12 min), while the Costa Rica sounding had the longest period of ~40 min. The Corpus Christi and Panama soundings had ~20 and ~25-min periods, respectively. Several different factors could explain this variation:

- Balloon size and shape
  The shape of the balloon will impact the drag force on the balloon as it moves through the air mass, with more flattened balloons experiencing more drag than vertically oblong balloons, as the drag force will scale with the effective cross-sectional area of the balloon. The shape of the balloon will also impact the ease with which melting ice falls off the balloon, with the vertically stretched balloons being able to eliminate ice mass faster than horizontally flattened balloons. The size of the balloon correlates with the available surface area for the accumulation of ice. Without cameras attached to the payload and recording the shape and size of the balloon with time, these speculative factors cannot be determined.
- Differences in mass of the balloon-payload systems
  The Houston sounding only included a radiosonde, while the others also included an ozonesonde. This lighter weight potentially leads to a faster oscillation as less ice is needed to cause the balloon to descend. The Costa Rica payload also included a CFH and had the largest mass, which could cause slower oscillation. The mass of the balloon contributes to the total mass of the balloon-payload system. More massive objects have greater inertia and require larger forces to result in the same acceleration. Figure 12 shows a roughly linear relationship between the mass of the balloon package and the duration of the oscillation from the four cases shown.

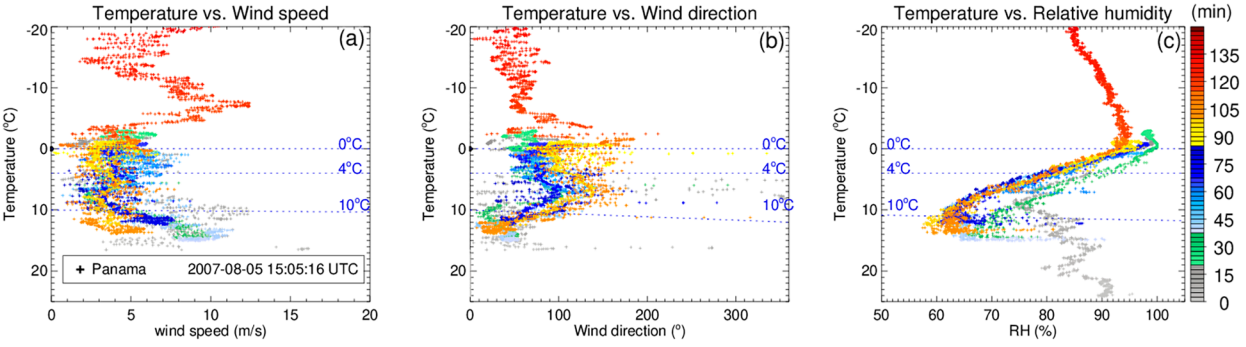

FIG. 9. Scatterplots of the (a) wind speed, (b) wind direction, and (c) relative humidity as a function of temperature during flights over Panama. The color bars in (a)–(c) represent the time after the launch.

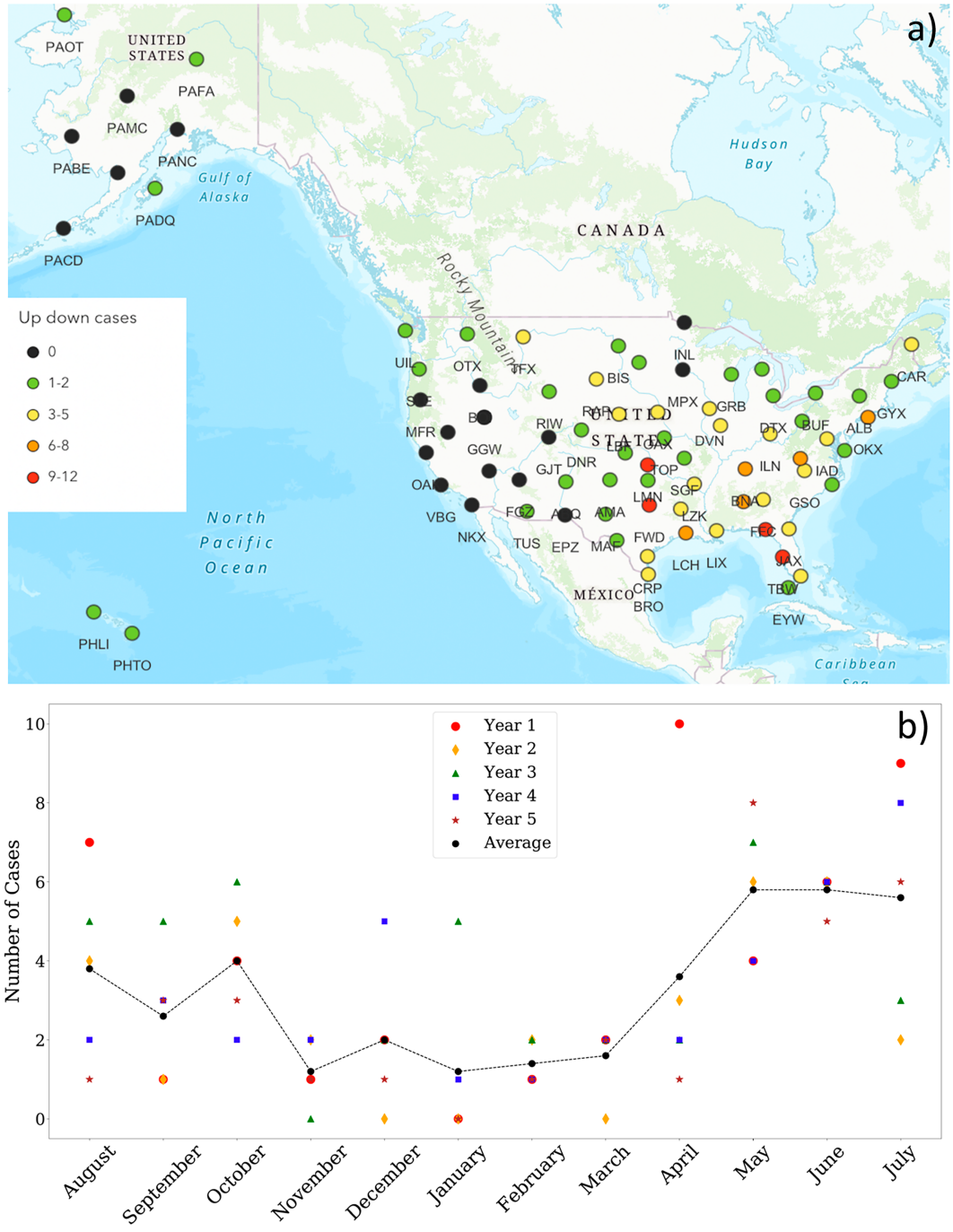

FIG. 10. (a) Map showing the number of potential up–down-oscillating cases for 78 NWS stations over a 5-yr period. (b) Annual trends (August–July) of potential up–down-oscillating cases from National Weather Service launches in the United States from 2016 to 2021.

However, more samples are needed to really understand the relationship between the mass of balloon payload and oscillation time.

- Wind shear
  A large change in wind speed and direction during the oscillation could impact the speed of the balloon as well as the accumulation of the ice mixture. Wind could help remove the ice as melting starts, hastening the return to an ascent.
- Rate of ice accumulation
  The icing rate could vary significantly depending on the temperature and amount of ice particles and supercooled liquid.

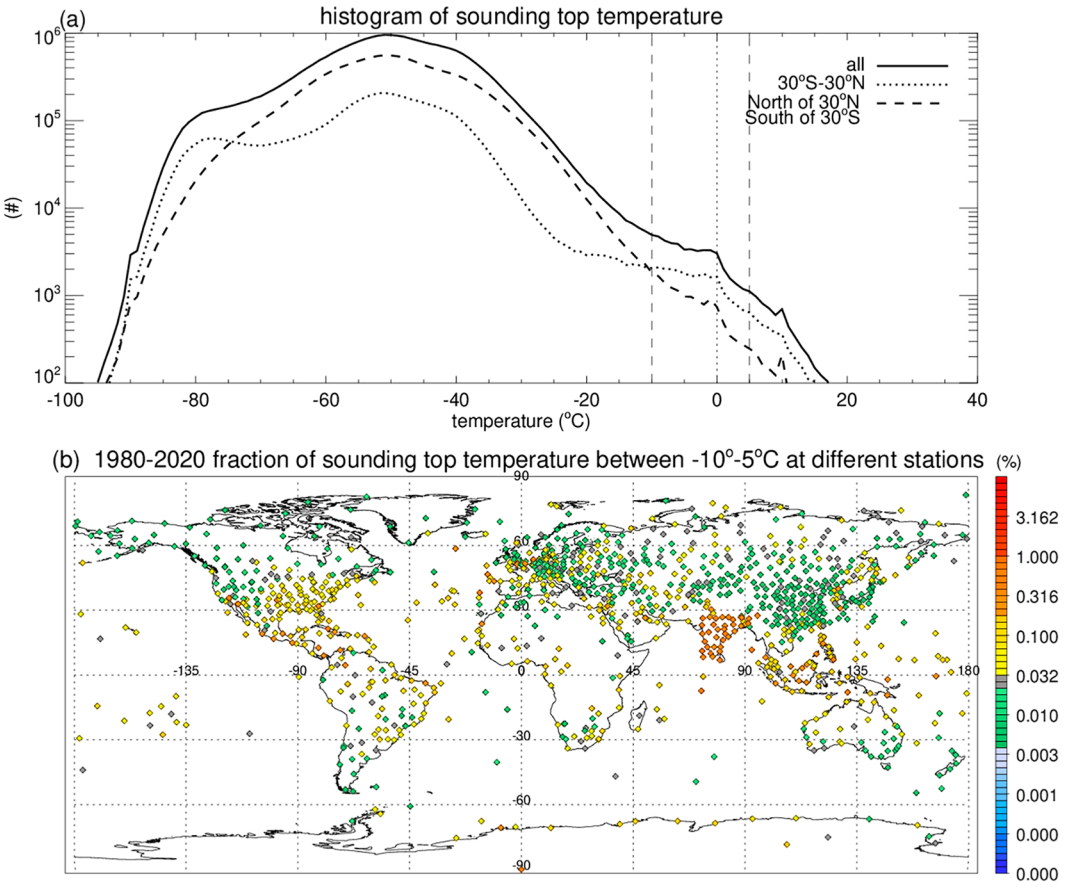

FIG. 11. (a) Histogram of the coldest temperature from profiles measured by radiosondes from 1980 to 2020 around the globe. (b) Fraction of the soundings' top temperatures between −10° and 5°C at each station with at least 10 000 sounding records.

However, it is quite difficult to directly measure the supercooled liquid water within clouds, except for limited cases of in situ observations (e.g., Rosenfeld and Woodley 2000). Therefore, the icing rate in different cloud regions and various types of clouds is still largely unknown. In this paper, we have demonstrated that, given the detailed information on the ascent and descent rates of oscillating balloons, it is possible to estimate the icing rate with some assumptions. Further in situ observations of liquid water content and supercooled liquid water content are needed to explore this hypothesis.

- Uncertainties in the measurements during the icing conditions

  Icing can cause the sensors to malfunction and provide inaccurate measurements as discussed in Waugh and Schuur (2018). For the events shown in this study, the temperature measurements are most likely credible because of the consistent lapse rate during the ascending and descending paths (Fig. 1). The GPS altitude is an independent measurement from icing (GPS module either collect GPS signal and calculate an altitude or report no signal). During all four events, the temperature values and altitude values vary consistently. If there is any bias in the temperature during the oscillation, different lapse rates would be observed between ascending and descending paths. However, there is no validation of relative humidity measurements, which could be influenced by icing. Also, during the icing, the additional weight to the balloon package would reduce the sensitivity to the wind variations. For an ozonesonde, the icing could block the inlet tube and lead to incorrect sensor responses.

In general, the differences in oscillation periods can most likely be explained by the mass of the payload. All launches took place during different levels of precipitation and wind, which can impact the balloon's behavior, with different teams taking part in each launch. Other than the period and number of oscillations, the behavior of each sounding was very similar, and therefore it would be interesting to analyze more cases. Collecting radiosonde data within a highly varying environment can provide important insight to improve weather forecasting during rainstorms. Currently, weather balloon launches conducted by the National Weather Service (NWS) are programmed only to collect data while the balloon is ascending and stop whenever the balloon starts to descend. This practice maintains consistent measurements among all radiosonde sites to feed into

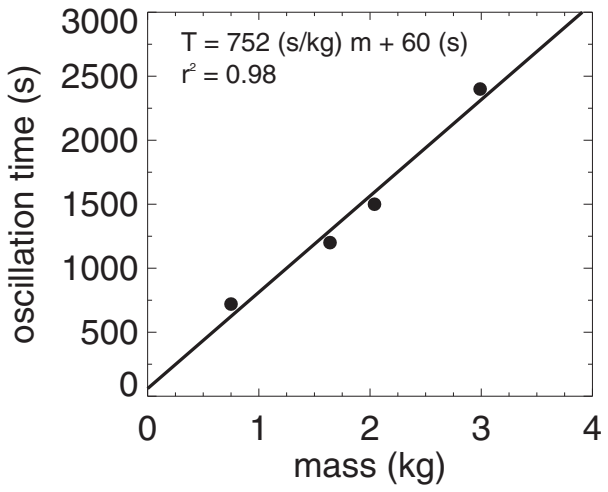

FIG. 12. Approximate oscillation period for the four flights described in this paper as a function of the approximate mass of the payload and balloon, which shows a linear relationship.

numerical models. A balloon that has oscillated a number of times due to ice accumulation and melting would have a delayed final ascent to a normal burst altitude where the balloon has likely drifted a long distance, and thus may not be as representative to the status of atmosphere at the dedicated time and location. However, if NWS soundings would keep tracking descent data, the profiles in the upper atmosphere could still be collected for these oscillating cases. Also, these oscillating cases provide unique icing information that can help improve our understanding of ice microphysics, which is critical for aviation safety.

Acknowledgments. We thank two anonymous reviewers for valuable suggestions that significantly improved the quality of this manuscript. This research was funded by the NASA DCOTSS program under Grant 80NSSC19K0346. The MRR radar is supported by NASA PMM program under Grant 80NSSC22K0591. We thank the workshop trainees who launched the ozonesonde on the morning of 8 July 2021 and Texas A&M University–Corpus Christi for hosting the ozonesonde workshop.

Data availability statement. The satellite infrared brightness temperature data are available at NASA GES DISC Center with https:doi.org/10.5067/P4HZB9N27EKU as cited in Janowiak et al. (2017). The radar data, including NPOL, MRMS, and MMR for two cases, and radiosonde data are available at Texas A&M–Corpus Christi upon request.

APPENDIX

Icing Rate Estimation

To estimate the icing rate on the surface of the balloon and ozonesonde package, we rely on the relationship between the ice mass buildup and the vertical acceleration of the package. Based on Newton's second law, the lift, weight of the package, including ice accumulation, and the air drag determines the acceleration of the package as written in Eq. (1):

$$(M_{\text{balloon}} + M_{\text{helium}} + M_{\text{instrument}} + M_{\text{water}} + M_{\text{ice}})a(t) = L + [M_{\text{instrument}} + M_{\text{water}} + M_{\text{ice}}(t)]g - \frac{1}{2}C_d|w(t)|w(t)A(t)\rho(t), \quad (1)$$

where $M_{\text{ice}}(t)$ is the mass of ice buildup as a function of time; $a(t)$ is the acceleration calculated with the velocity change with time; L is the payoff weight while inflating the balloon (i.e., 2 kg multiplied by $|g|$); M_{balloon} is the mass of balloon (i.e., 0.8 kg); M_{helium} is the mass of helium that can be estimated by $M_{\text{helium}} = 4(L/|g| + M_{\text{balloon}})/24.9$; $M_{\text{instrument}}$ is mass of instrument package including ozone and radio sondes, parachute, payout reel, and strings; M_{water} is the mass of rainwater accumulated on the package because the sonde passed through rain; g is gravitation constant with value -9.8 m s^{-2}; $w(t)$ is the vertical velocity of the sonde; and $A(t)$ is the surface area of the whole balloon system, including the area of the instrument, parachute, payout reel, and balloon. The surface area of the balloon A_{balloon} changes with air pressure. The value of $A_{\text{balloon}}(t)$ can be estimated as the function of air pressure $P(t)$ and temperature $T(t)$ by $A_{\text{balloon}}(t) = 4\pi\{[3/(4\pi)][22.4M_{\text{helium}}P_sT(t)]/[4P(t)T_s]\}^{2/3}$, where P_s is standard air pressure at sea level; T_s is surface temperature, $\rho(t)$ is the air density, which can be calculated with the temperature and pressure measurements from the radiosonde; and C_d is the air drag coefficient.

From Eq. (1), we can derive Eq. (2) to estimate $M_{\text{ice}}(t)$ along the balloon trajectory:

$$M_{\text{ice}}(t) = \frac{1}{a(t) + g}\left[L + (M_{\text{instrument}} + M_{\text{water}})g - (M_{\text{balloon}} + M_{\text{heluim}} + M_{\text{instrument}} + M_{\text{water}})a(t) - \frac{1}{2}C_d|w(t)|w(t)A(t)\rho(t)\right]. \quad (2)$$

There are two unknowns in Eq. (2). One is the amount of water M_{water} on the package. Sensitivity tests conducted on water amounts between 0 and 200 g showed that the mass of water did not significantly change the result. However, the other unknown, the air drag coefficient C_d for the irregular shape of the balloon and instruments, is critical in the calculation. Wang et al. (2009) demonstrated the complexity of the drag force associated with balloon and radiosonde. In our case, the instrument package, including balloon, ozonesonde, radiosonde, parachute, drop reel and attached strings, and deformation of balloon during the icing make the direct estimation of drag coefficient difficult. To solve this problem, we subjectively adjusted the C_d parameter to keep the M_{ice} close to 0 in the legs with uprising from warmer temperature to the freezing level assuming ice fully melted while the balloon was rising. For the case of Corpus Christi, the optimum drag coefficient C_d with a value of 0.13 is chosen to derive M_{ice}.

REFERENCES

Ciesielski, P. E., and Coauthors, 2014: Quality-controlled upper-air sounding dataset for DYNAMO/CINDY/AMIE: Development and corrections. *J. Atmos. Oceanic Technol.*, **31**, 741–764, https://doi.org/10.1175/JTECH-D-13-00165.1.

Dirksen, R. J., M. Sommer, F. J. Immler, D. F. Hurst, R. Kivi, and H. Vömel, 2014: Reference quality upper-air measurements: GRUAN data processing for the Vaisala RS92 radiosonde. *Atmos. Meas. Tech.*, **7**, 4463–4490, https://doi.org/10.5194/amt-7-4463-2014.

Durre, I., R. S. Vose, and D. B. Wuertz, 2006: Overview of the integrated global radiosonde archive. *J. Climate*, **19**, 53–68, https://doi.org/10.1175/JCLI3594.1.

——, X. Yin, R. S. Vose, S. Applequist, and J. Arnfield, 2018: Enhancing the data coverage in the integrated global radiosonde archive. *J. Atmos. Oceanic Technol.*, **35**, 1753–1770, https://doi.org/10.1175/JTECH-D-17-0223.1.

Gaffen, D. J., 1994: Temporal inhomogeneities in radiosonde temperature records. *J. Geophys. Res.*, **99**, 3667–3676, https://doi.org/10.1029/93JD03179.

Gultepe, I., and Coauthors, 2019: A review of high impact weather for aviation meteorology. *Pure Appl. Geophys.*, **176**, 1869–1921, https://doi.org/10.1007/s00024-019-02168-6.

Hersbach, H., and Coauthors, 2020: The ERA5 global reanalysis. *Quart. J. Roy. Meteor. Soc.*, **146**, 1999–2049, https://doi.org/10.1002/qj.3803.

Holdridge, D., 2020: Balloon-Borne Sounding System (SONDE) instrument handbook. ARM Tech. Rep. DOE/SC-ARM-TR-029, DOE, 38 pp.

Homeyer, C., J. Smith, T. Bui, J. Dean-Day, T. Hanisco, R. Hannun, J. St Clair, and K. Bedka, 2023: A case study of the highest ever altitude of in situ observations of convective hydration of the stratosphere during the DCOTSS field campaign. *2023 EGU General Assembly*, Vienna, Austria, European Geosciences Union, Abstract EGU23-9858, https://doi.org/10.5194/egusphere-egu23-9858.

Houze, R. A., Jr., 2018: 100 years of research on mesoscale convective systems. *A Century of Progress in Atmospheric and Related Sciences: Celebrating the American Meteorological Society Centennial*, *Meteor. Monogr.*, No. 59, Amer. Meteor. Soc., https://doi.org/10.1175/AMSMONOGRAPHS-D-18-0001.1.

Hurst, D. F., and Coauthors, 2011: Comparisons of temperature, pressure and humidity measurements by balloon-borne radiosondes and frost point hygrometers during MOHAVE-2009. *Atmos. Meas. Tech.*, **4**, 2777–2793, https://doi.org/10.5194/amt-4-2777-2011.

Janowiak, J. E., R. J. Joyce, and Y. Yarosh, 2001: A real-time global half-hourly pixel-resolution infrared dataset and its applications. *Bull. Amer. Meteor. Soc.*, **82**, 205–218, https://doi.org/10.1175/1520-0477(2001)082<0205:ARTGHH>2.3.CO;2.

——, B. Joyce, and P. Xie, 2017: NCEP/CPC L3 half hourly 4km global (60S–60N) merged IR V1. Goddard Earth Sciences Data and Information Services Center (GES DISC), accessed August 2022, https://doi.org/10.5067/P4HZB9N27EKU.

Klugmann, D., K. Heinsohn, and H. Kirzel, 1996: A low cost 24 GHz FM-CW Doppler radar rain profiler. *Contrib. Atmos. Phys.*, **69**, 247–253.

Komhyr, W. D., 1969: Electrochemical concentration cells for gas analysis. *Ann. Geophys.*, **25**, 203–210.

Miloshevich, L. M., H. Vömel, D. N. Whiteman, and T. Leblanc, 2009: Accuracy assessment and correction of Vaisala RS92 radiosonde water vapor measurements. *J. Geophys. Res.*, **114**, D11305, https://doi.org/10.1029/2008JD011565.

Morris, G. A., A. M. Thompson, K. E. Pickering, S. Chen, E. J. Bucsela, and P. A. Kucera, 2010: Observations of ozone production in a dissipating tropical convective cell during TC4. *Atmos. Chem. Phys.*, **10**, 11 189–11 208, https://doi.org/10.5194/acp-10-11189-2010.

Nesbitt, S. W., and E. J. Zipser, 2003: The diurnal cycle of rainfall and convective intensity according to three years of TRMM measurements. *J. Climate*, **16**, 1456–1475, https://doi.org/10.1175/1520-0442(2003)016%3C1456:TDCORA%3E2.0.CO;2.

Ramella Pralungo, L., L. Haimberger, A. Stickler, and S. Brönnimann, 2014: A global radiosonde and tracked balloon archive on 16 pressure levels (GRASP) back to 1905—Part 1: Merging and interpolation to 00:00 and 12:00 GMT. *Earth Syst. Sci. Data*, **6**, 185–200, https://doi.org/10.5194/essd-6-185-2014.

Rosenfeld, D., and W. L. Woodley, 2000: Deep convective clouds with sustained supercooled liquid water down to −37.5°C. *Nature*, **405**, 440–442, https://doi.org/10.1038/35013030.

Schrab, K., and D. B. Caldwell, 2010: National weather service manual 10-1401: Operations and services, upper air program NWSPD 10-14, rawinsonde observations. Tech. Rep. NWSM 10-1401, 208 pp., https://www.nws.noaa.gov/directives/sym/pd01014001curr.pdf.

Smit, H. G. J., A. M. Thompson, and ASOPOS Panel, 2021: Ozonesonde measurement principles and best operational practices: ASOPOS 2.0 (Assessment of standard operating procedures for ozone sondes). WMO/GAW Rep. 268, WMO, 173 pp., https://library.wmo.int/doc_num.php?explnum_id=10884.

Smith, T. M., and Coauthors, 2016: Multi-Radar Multi-Sensor (MRMS) severe weather aviation products: Initial operating capabilities. *Bull. Amer. Meteor. Soc.*, **97**, 1617–1630, https://doi.org/10.1175/BAMS-D-14-00173.1.

Theisen, C. J., P. A. Kucera, and M. R. Poellot, 2009: A study of relationships between Florida thunderstorm properties and corresponding anvil cloud characteristics. *J. Appl. Meteor. Climatol.*, **48**, 1882–1901, https://doi.org/10.1175/2009JAMC1991.1.

Toon, O. B., and Coauthors, 2010: Planning, implementation, and first results of the Tropical Composition, Cloud and Climate Coupling Experiment (TC4). *J. Geophys. Res.*, **115**, D00J04, https://doi.org/10.1029/2009JD013073.

van Oldenborgh, G. J., and Coauthors, 2018: Corrigendum: Attribution of extreme rainfall from Hurricane Harvey, August 2017. *Environ. Res. Lett.*, **13**, 019501, https://doi.org/10.1088/1748-9326/aaa343.

Vömel, H., and Coauthors, 2007: Accuracy of tropospheric and stratospheric water vapor measurements by the cryogenic frost point hygrometer: Instrumental details and observations. *J. Geophys. Res.*, **112**, D08305, https://doi.org/10.1029/2007JD008698.

von Rohden, C., M. Sommer, T. Naebert, V. Motuz, and R. J. Dirksen, 2022: Laboratory characterisation of the radiation temperature error of radiosondes and its application to the GRUAN data processing for the Vaisala RS41. *Atmos. Meas. Tech.*, **15**, 383–405, https://doi.org/10.5194/amt-15-383-2022.

Wang, J., and L. Zhang, 2008: Systematic errors in global radiosonde precipitable water data from comparisons with ground-based GPS measurements. *J. Climate*, **21**, 2218–2238, https://doi.org/10.1175/2007JCLI1944.1.

——, J. Bian, W. O. Brown, H. Cole, V. Grubišić, and K. Young, 2009: Vertical air motion from T-REX radiosonde and

dropsonde data. *J. Atmos. Oceanic Technol.*, **26**, 928–942, https://doi.org/10.1175/2008JTECHA1240.1.

Waugh, S., and T. J. Schuur, 2018: On the use of radiosondes in freezing precipitation. *J. Atmos. Oceanic Technol.*, **35**, 459–472, https://doi.org/10.1175/JTECH-D-17-0074.1.

Yoneyama, K., C. Zhang, and C. N. Long, 2013: Tracking pulses of the Madden–Julian oscillation. *Bull. Amer. Meteor. Soc.*, **94**, 1871–1891, https://doi.org/10.1175/BAMS-D-12-00157.1.

Zhang, J., and Coauthors, 2016: Multi-Radar Multi-Sensor (MRMS) quantitative precipitation estimation: Initial operating capabilities. *Bull. Amer. Meteor. Soc.*, **97**, 621–638, https://doi.org/10.1175/BAMS-D-14-00174.1.

Zipser, E. J., D. J. Cecil, C. Liu, S. W. Nesbitt, and D. P. Yorty, 2006: Where are the most intense thunderstorms on Earth? *Bull. Amer. Meteor. Soc.*, **87**, 1057–1072, https://doi.org/10.1175/BAMS-87-8-1057.